Physics of Plasmas ARTICLE pubs.aip.org/aip/pop

Experimental and computational study of phase space dynamics in strongly coupled plasmas with steep density gradients

Cite as: Phys. Plasmas **32**, 032104 (2025); doi: 10.1063/5.0253054
Submitted: 13 December 2024 · Accepted: 7 February 2025 ·
Published Online: 5 March 2025

Scott Bergeson,[1,a)] Matthew Schlitters,[1] Matthew Miller,[1] Ben Farley,[1] Devin Sieverts,[1] Michael S. Murillo,[2] and Jeffrey R. Haack[3]

AFFILIATIONS

[1]Department of Physics and Astronomy, Brigham Young University, Provo, Utah 84602, USA
[2]Department of Computational Mathematics, Science and Engineering, Michigan State University, East Lansing, Michigan 48824, USA
[3]Computational Physics and Methods Group, Los Alamos National Laboratory, Los Alamos, New Mexico 87545, USA

[a)]Author to whom correspondence should be addressed: scott.bergeson@byu.edu

ABSTRACT

Understanding how plasmas thermalize when density gradients are steep remains a fundamental challenge in plasma physics, with direct implications for fusion experiments and astrophysical phenomena. Standard hydrodynamic models break down in these regimes, and kinetic theories make predictions that have never been directly tested. Here, we present the first detailed phase-space measurements of a strongly coupled plasma as it evolves from sharp density gradients to thermal equilibrium. Using laser-induced fluorescence imaging of an ultracold calcium plasma, we track the complete ion distribution function $f(\mathbf{x}, \mathbf{v}, t)$. We discover that commonly used kinetic models (Bhatnagar–Gross–Krook and Lenard–Bernstein) overpredict thermalization rates, even while correctly capturing the initial counterstreaming plasma formation. Our measurements reveal that the initial ion acceleration response scales linearly with electron temperature, and that the simulations underpredict the initial ion response. In our geometry we demonstrate the formation of well-controlled counterpropagating plasma beams. This experimental platform enables precision tests of kinetic theories and opens new possibilities for studying plasma stopping power and flow-induced instabilities in strongly coupled systems.

I. INTRODUCTION

Hydrodynamic models accurately predict plasma transport when the mean free path is shorter than the plasma scale length.[1–4] This capability is critical for experiment planning, data analysis, plasma characterization, and parameter optimization.[5] Radiation-hydrodynamic codes like LILAC,[6] HYDRA,[7] and xRAGE[8] have been shown to successfully capture the temperature, density, and neutron yield of experiments at NIF and OMEGA. They nicely model the influence of target surface defects, voids, and structural imperfections on ICF neutron yield in the hydrodynamic limit.[9,10] Hydrodynamic codes are widely used because they are much faster than kinetic codes and incorporate radiation effects much more easily.[11]

However, many plasmas start far from the hydrodynamic limit.[12] Kinetic effects arise when the velocity distributions are strongly non-Maxwellian, which is the inevitable outcome of nearly every laser–matter interaction, including laser direct-drive experiments. In some cases, when experiment and simulation are directly compared, hydrodynamic codes do not reproduce the experiments even though the hydrodynamic limit is reached,[13] suggesting the presence of kinetic effects outside the hydrodynamic approximation. In models of laser direct-drive experiments at OMEGA, for example, understanding kinetic effects is critical.[6]

Kinetic codes derive from the plasma kinetic equation

$$\frac{\partial f}{\partial t} + \mathbf{v} \cdot \nabla_{\mathbf{x}} f + \frac{q\mathbf{E}}{m} \cdot \nabla_{\mathbf{v}} f = \mathscr{C}[f], \tag{1}$$

where $f(\mathbf{x}, \mathbf{v}, t)$ is the distribution function for a particular ion species of mass m, and $\mathbf{E}$ represents the electric field. Given a model of the collision operator $\mathscr{C}$, the kinetic equation can be solved for the distribution function $f(\mathbf{x}, \mathbf{v}, t)$. When the distribution function is near

Maxwellian, one can derive hydrodynamic models by taking velocity moments of Eq. (1). Validating the various collision operator models and determining when the hydrodynamic approximation is appropriate is as an ongoing and important concern in many areas of plasma science.

In a series of papers, Killian's group at Rice University studied the kinetic-to-hydrodynamic transition using ultracold neutral plasmas (UNPs).[14–16] By placing a series of obstructions in the ionizing laser beam, those authors created a UNP with "sculpted" initial conditions.[17] They found that UNPs with sharp and deep density gradients produced non-thermal ion velocity distributions. They explored the evolution of a UNP with a gap in the middle. Their gap had sharp edges, leading to ion jetting across the gap. They compared their results to a hydrodynamic code and found that shallower gradients, smaller gaps, and lower initial electron temperatures led to more hydrodynamic behavior.

In this paper, we take a closer look at the kinetic-to-hydrodynamic evolution of a UNP with steep density gradients. We create a strongly coupled calcium UNP with steep density gradients. Using precision laser spectroscopy, we determine the plasma ion phase space distribution function. We compare these distributions with predictions from a kinetic code that uses two different collision operators. We find that our simulations generally reproduce plasma behavior, with significant differences in the approach to equilibrium. The kinetic codes rely primarily on low-order moments of the distribution functions and do not capture all of the observed phase-space dynamics. This platform enables precision tests of kinetic theories and opens new possibilities for studying plasma stopping power and flow-induced instabilities in strongly coupled systems.

II. UNPs AND HEDPs

The UNP environment serves as an efficient high energy-density plasma (HEDP) simulator.[18] The connection lies in the Yukawa model.[19,20] In general, HEDPs and UNPs are multicomponent plasmas in which pairwise ion interactions can be approximated using a screened, repulsive $1/r$ potential

$$V(r_{ij}) = \frac{Z_i Z_j e^2}{r_{ij}} \exp\left(-\frac{r_{ij}}{\lambda}\right), \tag{2}$$

where Z and Z_j are the (effective) ionization states of ions i and j, and r_{ij} is the distance between them. In this model, electrons serve as a neutralizing background charge, screening ion charges with a characteristic length λ. The screening length is often taken to be the Debye length $\lambda_D = [k_B T_e \varepsilon_0/(ne^2)]^{1/2}$, where n is the electron density and T_e is the electron temperature. However, other formulations of this length include ion screening and quantum and strong-coupling effects.[21]

The Yukawa model does not capture all of the expected physics in HEDPs or UNPs. Electron-ion thermalization,[22–33] for example, is not explicitly included in the Yukawa model. Quantum effects,[34,35] such as bound states, three-body recombination, and quantum degeneracy, are also not included. HEDPs and UNPs share similar physics in these non-Yukawa aspects as well.

When the Yukawa model is valid, two parameters uniquely define the plasma state.[36,37] One is the unscreened strong-coupling parameter

$$\Gamma = \frac{Z^2 e^2}{a_{\rm ws}} \frac{1}{k_B T}, \tag{3}$$

where $a_{\rm ws} = (3/4\pi n_i)^{1/3}$ is the Wigner–Seitz radius (ion sphere radius), n_i is the ion density, and T is the ion temperature. The other is the inverse scaled screening length

$$\kappa = \frac{a_{\rm ws}}{\lambda}, \tag{4}$$

where λ is once again the Yukawa screening length of Eq. (2). Both UNPs and HEDPs can be well-described by Yukawa interactions and exist in overlapping regions in the $\Gamma - \kappa$ parameter space.[18,21]

The Yukawa model is commonly used to describe ion–ion interactions in both weakly and strongly coupled plasmas.[19,36] Examples of strongly-coupled plasmas with $\Gamma > 1$ include white dwarf stars,[38] the cores of Jovian planets,[39,40] some stages of laser-driven plasma experiments[6,41] and X- and Z-pinch plasmas,[42] dusty plasmas,[43,44] quark-gluon plasmas,[45,46] dusty plasmas consisting of highly charged dust particles,[47–50] non-neutral plasmas,[51–53] ions in UNPs[54–56] and other systems.

Comparing model predictions with experimental data provides an important check of plasma theories in the strongly coupled plasma regime. The range of strong coupling parameter values accessible to UNPs[57] is in the range of $\Gamma \approx 2$. Using sculpted plasmas,[17] it is possible to create kinetic conditions that are far from equilibrium. When $\Gamma \ll 1$, collisions are described using small-angle scattering that leads to various prescriptions for Coulomb logarithms.[28,58] The Coulomb logarithm description can be extended up to $\Gamma \sim 1$ using a numerically computed binary cross sections.[21] Ultimately, for $\Gamma \gg 1$, one needs to include collective phenomena.[59]

Strong coupling also introduces new behaviors in the plasma that arise from spatial order. For example, the scaled viscosity displays a minimum near $\Gamma \sim 5$ to 10, increasing toward very large values of the strong coupling parameter.[21] As Γ increases toward 1, many-body hard collisions become important. The characteristic length scale changes from the Debye length to the inter-particle spacing. As Γ increases beyond $\Gamma = 10$ to greater coupling, viscosity increases again. Isolating transport processes in HEDPs is difficult because many different processes compete.[60,61] Ideally, a precision experiment which enables isolation of one or two simple processes would make it possible to evaluate theoretical treatments. UNPs provide such an opportunity in a range of Γ and κ relevant to HEDP experiments.[62]

III. EXPERIMENT

Three excellent reviews describe how UNPs are generated, diagnosed, and modeled.[54,55,63] UNPs are strongly coupled, non-degenerate, quasi-homogeneous, quasi-steady-state, $Z = 1$ plasmas with accurately known initial conditions.[64] They provide an idealized platform for measuring plasma transport properties,[18,64–70] and can be used to simulate transport in HEDPs.[16,18,57,71–77] Some studies in our lab include dynamics of strongly coupled neutral Coulomb systems,[78–81] exploring the HEDP/UNP crossover,[18,71] ion transport properties of binary ion mixtures,[64,65,72] and the density evolution of partially magnetized plasmas.[66,82,83]

Our UNPs are created by photo-ionizing laser-cooled Ca atoms in a magneto-optical trap (MOT).[64,66,72,84] The MOT is formed by overlapping six counterpropagating laser beams with an atomic beam in the center of a magnetic quadrupole field. Ionizing laser pulses at 423 and 390 nm form the Ca^+ plasma, as indicated in Figs. 1(a)–1(c). The difference of the ionization energy and the photon energy of the photo-ionizing laser sets the initial electron temperature, typically

$2\Delta E/3k_B = T_e = 10$–$400$ K. On the other hand, the initial ion temperature is determined by disorder-induced heating, usually $T_i = 1$ K, depending on the density.[78,85,86] When the ionizing lasers are spatially smooth, the density of the plasma equals the density of the neutral atom cloud, and it evolves self-similarly[87]

$$n(r,t) = \frac{n_0}{(1+t^2/\tau_e^2)^{3/2}} \exp\left[-\frac{r^2}{2\sigma_0^2(1+t^2/\tau_e^2)}\right]. \quad (5)$$

The peak plasma density is in the range of $n_0 = 10^8$–10^{10} cm^{-3}, the initial rms size is $\sigma_0 \sim 1$ mm, and the characteristic expansion time is $\tau_e = [m\sigma_0^2/(k_B T_e)]^{1/2}$. The resulting plasma is just inside the strongly-coupled plasma regime with $\Gamma = 2$, although a range of $\Gamma = 0.1$–11 is possible.[57]

We analyze these plasmas using laser-induced fluorescence (LIF).[64,72,88] A probe laser beam tuned to the Ca^+ 397 nm resonance [Fig. 1(b)] is shaped to be 1 cm wide in the y-direction and 1 mm thick in the x-direction, and it is centered on the plasma [Fig. 1(c)]. Ion fluorescence in the illuminated portion of the plasma is imaged onto a gated ICCD camera, allowing us to record a cross-Sec. of the ion density distribution near the center of the plasma. The ICCD camera is triggered after a delay time of 0–20 μs and captures fluorescence during a short time window, typically between 25 and 200 ns. Identical plasmas are generated 10 times per second. To improve the signal-to-noise ratio, we repeatedly measure ion fluorescence on 50 sequentially created plasmas with identical measurement conditions.

We adjust the frequency of the probe laser beam in $\Delta f = 20$ MHz steps that span the entire velocity distribution. For ions moving at the appropriate velocity, the probe laser beam is Doppler-shifted into resonance, $v = \lambda \Delta f$, where λ is the atomic transition wavelength. The ICCD camera then records where ions at that velocity are located in the plasma. By analyzing the images at different probe laser frequencies, we are able to map out a spatially resolved ion distribution function at the chosen delay time. The Doppler shift provides information about the velocity component that is parallel to the probe laser beam propagation direction. The camera gives the location of those ions.

As shown in Fig. 1(d), we integrate the fluorescence image over a range of ± 0.5 mm in y to obtain a portion of the distribution function as a function of z at that ion velocity and time, $f(z, v_n, t_n)$, where v_n is the ion velocity Doppler-shifted into resonance with the probe laser beam and t_n is the delay time at which the image was taken. This y-integrated image becomes one row in the phase-space image of the plasma, showing where all the ions of that particular velocity are located in space. We repeat this measurement for a wide range of probe laser beam frequency detunings to generate the image shown in Fig. 1(e).

The image in Fig. 1(e) represents the convolution of the true distribution function with the Lorentzian linewidth of the Ca^+ 397 nm transition. The convolution appears in both velocity v and position z due to hydrodynamic flow in the z direction. Deconvolving the images is challenging due to the non-trivial hydrodynamic velocity distribution in sculpted plasmas.

We generate sculpted plasmas[17] by spatially structuring the ionizing laser beam. We place a wire in the ionizing laser, directly in front of a lens pair. The wire is 1:1 imaged into the plasma and the ionizing laser beam is nearly collimated at the plasma[82] when the lenses are identical, spaced by $2f$, and the wire-to-plasma distance is $4f$. For this work, we use a pair of 200-mm focal length UV-achromatic lenses to image the wire onto the plasma. The plasma forms as the optical "negative" of the wire. A wire is imaged as a sheet at the plasma, creating two hemispherical plasmas separated by a sharp-edged gap. For the data shown in this paper, our wire diameter and the plasma gap are both 0.28 mm.

In our experiment, we collect fluorescence images when the probe laser beam propagates both parallel and perpendicular to the direction of the density gradient. In this way, we generate information about $f(y, v_y, t)$ and $f(z, v_z, t)$. Due to the symmetry of our experiment, $f(x, v_x, t) = f(y, v_y, t)$.

IV. MULTI-SPECIES KINETIC MODELING

Kinetic models track particle distributions in phase space. They accommodate non-equilibrium flow features such as e.g., bump-on-tail interactions, two stream instabilities. The cost is that they are more

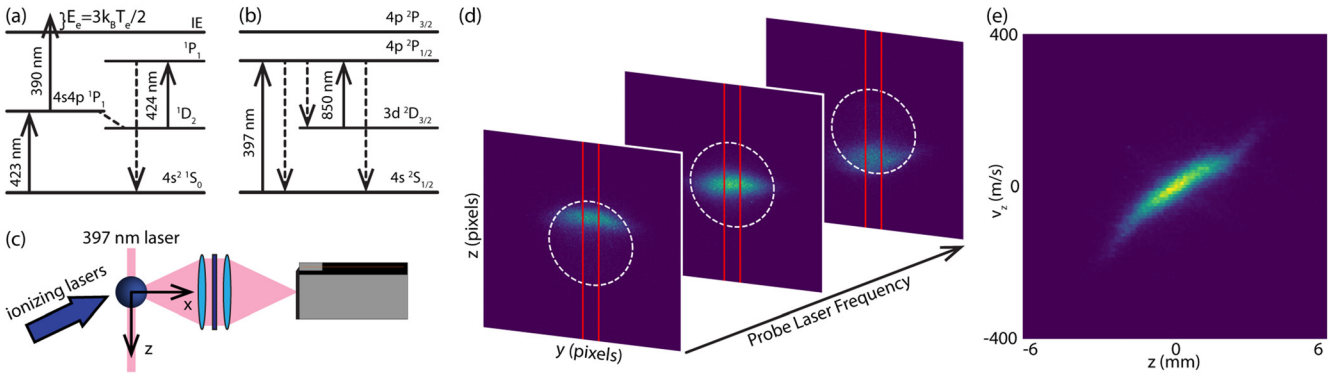

FIG. 1. Generating the phase space fluorescence maps. (a) Partial energy level diagram for Ca. The wavelength of the 390 nm laser determines the electron energy. (b) Partial energy level diagram for Ca^+. (c) Schematic representation of fluorescence measurements. A pair of lenses collects plasma fluorescence and images it onto an ICCD camera sensor. A spectral filter is used to isolate only the 397 nm fluorescence. (d) Images at $\Delta f = -200, 0, +200$ MHz, which yields the v_z information. Camera images show ions Doppler-shifted into resonance with the probe laser beam. Dashed white lines indicate the physical size of the plasma ($r = 2\sigma_0$). Red lines indicate the one-dimensional slice in z, with velocity information coming from Δf. (e) Phase space fluorescence map. Plasma conditions: $n_0 = 1.3 \times 10^9$ cm^3, $T_e = 96$ K, $T_i = 1$ K, $\sigma_0 = 1.29$ mm, delay time $= 4$ μs, measurement window $= 200$ ns.

computationally expensive than hydrodynamic models due to their higher dimensionality.

A. Collision models

We use two collision operators in our kinetic code: the Bhatnagar–Gross–Krook (BGK)[89–91] and the Lenard–Bernstein (LB)[92] models.

The BGK collision term in Eq. (1) has the form

$$\mathscr{C}^{\mathrm{BGK}}[f] = \frac{\mathscr{M}(\mathbf{x},\mathbf{v},t) - f(\mathbf{x},\mathbf{v},t)}{\tau(\mathbf{x},t)}, \tag{6}$$

where the equilibrium Maxwellian distribution is

$$\mathscr{M}(\mathbf{x},\mathbf{v},t) = n(\mathbf{x},t)\exp\left[-\frac{(\mathbf{u}(\mathbf{x},t)-\mathbf{v})^2}{2v_{\mathrm{th}}^2(\mathbf{x},t)}\right]. \tag{7}$$

Here, $n(\mathbf{x},t)$ describes the spatial distribution, $v_{\mathrm{th}}^2(\mathbf{x},t) = k_B T(\mathbf{x},t)/m$ is the ion thermal velocity, equal to the second central moment of the ion velocity distribution, and $\mathbf{u}(\mathbf{x},t)$ is the local average flow velocity. The parameter $\tau(\mathbf{x},t)$ is the characteristic relaxation time for the system. It includes effects of ion thermalization, mixing, electron-ion collisions, viscosity, and other transport properties.

We explore the importance of velocity diffusion by using a different collision operator. Following the work of Lenard and Bernstein,[92] we set the right-hand side of Eq. (1) to

$$\mathscr{C}^{\mathrm{LB}} = \frac{1}{\tau(\mathbf{x},t)}\frac{\partial}{\partial \mathbf{v}}\cdot\left[\mathbf{v}f(\mathbf{x},\mathbf{v},t) + v_{\mathrm{th}}^2(\mathbf{x},t)\frac{\partial f(\mathbf{x},\mathbf{v},t)}{\partial \mathbf{v}}\right]. \tag{8}$$

For both collision models, the collision times τ are a free parameter that can be tuned to match specific properties, e.g., temperature or momentum relaxation rates. In this work, the Ion–ion τ are chosen to match temperature relaxation using the Stanton–Murillo Transport (SMT) cross sections,[21] which are valid into moderately coupled plasma regimes. These collision frequencies, as well as the derivations of the BGK and LB forms of the collision operator themselves, implicitly rely on the assumption that the distribution functions are near Maxwellian; however, they are favored for their simplicity relative to the much more computationally expensive Boltzmann or Fokker–Planck models.

B. Electric field

The electric field in Eq. (1) is modeled through a nonlinear Poisson–Boltzmann model, where

$$n_e(\mathbf{x},t) = n_{e0}\exp[e\phi(\mathbf{x},t)/k_B T_e(\mathbf{x},t)], \tag{9}$$

$$\mathbf{E}(\mathbf{x},t) = -\nabla\phi(\mathbf{x},t), \tag{10}$$

where n_{e0} is a normalization constant that ensures charge neutrality. Using the Poisson equation for the electric field, this results in the nonlinear equation

$$-\nabla^2\phi = 4\pi e[Zn - n_{e0}\exp(e\phi/k_B T_e)], \tag{11}$$

where Z is the charge of the ion particles; in this study, we have $Z = 1$.

The electron-ion temperature relaxation is modeled with an additional set of equations for the electrons

$$\frac{\partial T_e(\mathbf{x},t)}{\partial t} + \frac{2e}{3k_B}\mathbf{u}(\mathbf{x},t)\cdot\mathbf{E}(\mathbf{x},t) = \frac{[T(\mathbf{x},t) - T_e(\mathbf{x},t)]}{\tau_{ei}(\mathbf{x},t)}, \tag{12}$$

and by adding an additional consistent electron-ion BGK collision term to the right hand side of Eq. (1),

$$\mathscr{C}^{\mathrm{ie}} = \frac{\mathscr{M}_{\mathrm{ie}}(\mathbf{x},\mathbf{v},t) - f(\mathbf{x},\mathbf{v},t)}{\tau_{ie}(\mathbf{x},t)}. \tag{13}$$

Here, the relaxation times τ_{ei}, τ_{ie} are given by standard Landau–Spitzer rates,[58] using GMS Coulomb Logarithms.[28] For more details on the formula for multispecies target distribution $\mathscr{M}_{ie}$, see Haack *et al.* on multi-species BGK operators.[90]

C. Code details

Our BGK model is a finite-volume, 1D-3V code capable of modeling multiple kinetic species.[93] We use $N_x = 496$ spatial grid points, each 5.2 μm wide, and $N_v = 100^3$ velocity grid points with a resolution of 2.8 m/s. The time step is 1 ns. The ions are the single kinetic species. The simulation is initialized with the experimentally measured $f(y, v_y, 0)$ and $f(z, v_z, 0)$.

The ion distribution function is evolved using Eq. (1) with collision operators in either Eq. (6) or Eq. (8). We solve the kinetic equation in conjunction with Eqs. (10), (11), and (12). The nonlinear equation (11) is solved using a standard Newton–Raphson method.[93]

V. RESULTS

A. Ion distribution function evolution

Experimental and simulated distribution function results are shown in Fig. 2. The z-component of the distribution function, $f(z, v_z, t)$ is represented using a logarithmic false-color plot. An imperfection in the optical imaging system causes additional fluorescence to appear in the gap between the plasmas. This is most clearly evident in the first and second panels of Fig. 2(a), for 0.1 and 1.1 μs. We have verified that the ion density in the gap is less than 1% of the peak plasma density using an independent measurement. For these experimental data, the peak density is 1.2×10^9 cm^{-3}. The initial electron temperature is $T_e = 96$ K. The ion fluorescence is integrated over a 200 ns window centered on the time displayed in the plots.

The steepness of the density gradient at the edge of the gap can be inferred from ion acceleration measurements. If we assume that the ions are accelerated by the ambipolar field, the acceleration can be written as

$$a_z = -\frac{k_B T_e}{m_i}\frac{1}{n}\frac{\partial n}{\partial z}. \tag{14}$$

When $T_e = 96$ K, the measured acceleration is 10^9 m/s^2, suggesting a gradient length scale of

$$\ell = \left[\frac{1}{n}\frac{\partial n}{\partial z}\right]^{-1} = 20\ \mu\mathrm{m}. \tag{15}$$

This method of inferring the density gradient has some uncertainties. Our simulations indicate that both the gradient and the density contrast ratio in the gap influence the initial ion acceleration.

The experimental data are compared with the simulation in Figs. 2(b) and 2(c). Both the BGK and LB simulations reproduce the ion jetting and counterpropagating plasma flow at 1.1 and 3.1 μs. The

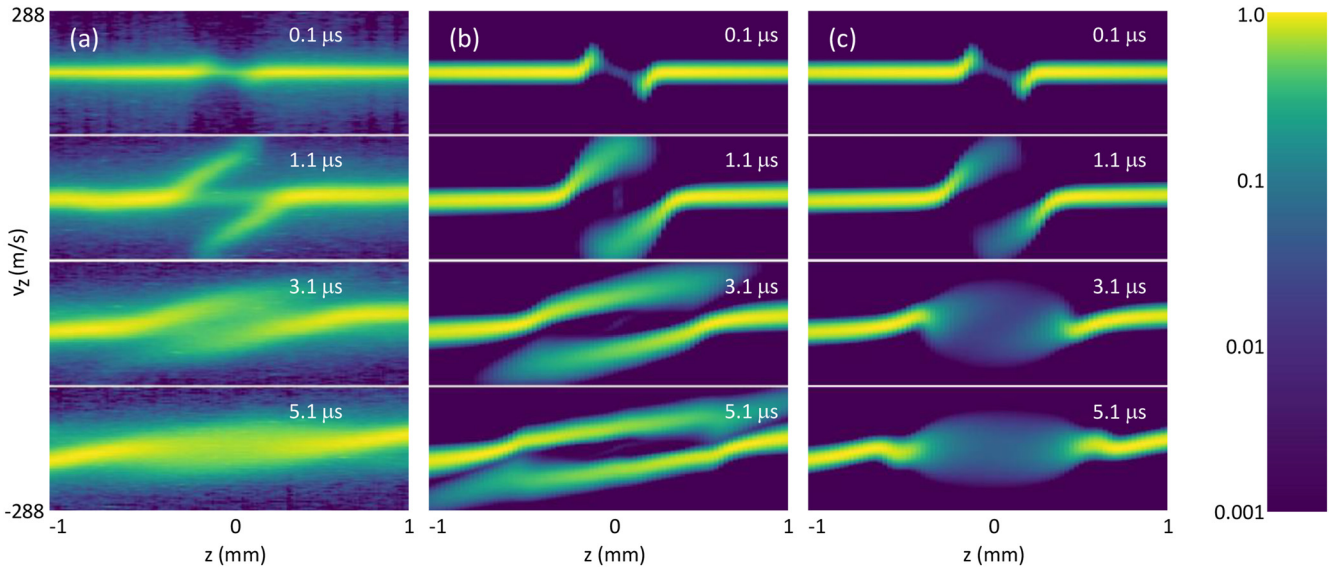

FIG. 2. The z-component of the ion distribution function on a logarithmic scale. (a) Experimental results. Because the experimental result derives from LIF, the underlying velocity distribution is convolved with the atomic linewidth. (b) Simulation with the BGK collision operator. (c) Simulation with the LB collision operator, Eq. (8).

thermalization rate in both simulations is somewhat slower than the experiment. Because the experimental inputs are well known, the simulations are tightly constrained. Referring to Eq. (1), only the terms on the right-hand side are in question. For kinetic codes, the parameters are the electron model, the collision frequency, and the form of the collision operator.

For the electron model, we use a Poisson–Boltzmann equation. The electrons are modeled as a fluid. We tried running the simulation treating the electrons as a second kinetic species. However, the large ion-to-electron mass ratio caused the simulation to run unacceptably slowly.

We vary the form of the collision operator using both BGK and LB collision operators, Eqs. (6) and (8). The primary difference is that the LB operator adds a velocity diffusion term. From the data in Fig. 2, this diffusion term speeds the approach to equilibrium, but in a way that doesn't precisely match the experimental data.

Varying the collision frequency also does not improve the agreement between the simulation and experiment. In both the BGK and LB simulation, decreasing the collision frequency decreases the thermalization rate. On the other hand, increasing the collision frequency dramatically decreases the ion jetting into the gap. Ions accelerate out from the two sides of the gap, collide in the middle without overlapping, and generate a broad Maxwellian velocity distribution. In addition, the increased collision frequency increases the pressure in the gap, restricting the plasma expansion at the gap edge.

B. Role of electron temperature in ion acceleration

The agreement between the experiment and simulations at 0.1 and 1.1 μs in Fig. 2 validates the electric field model described in Sec. IV B. At these times, when the relative ion velocities in the gap are high, we expect the ballistic motion and electric fields to dominate the evolution of the ion distribution making the collision terms negligible.

At even earlier times, the electrons may not be Maxwellian. Nonthermal electrons could race into the gap ahead of the ions, contributing to a greater electric field than predicted by our model.

We study this possibility by measuring the ion acceleration during the first 25 ns of plasma evolution. In the experiment, we set the camera delay time to 0 ns and the camera measurement duration to only $\Delta t = 25$ ns and measure the z-component of the ion distribution function, $f(z, v_z)$. From this we calculate the z-component of the hydrodynamic velocity as a function of z,

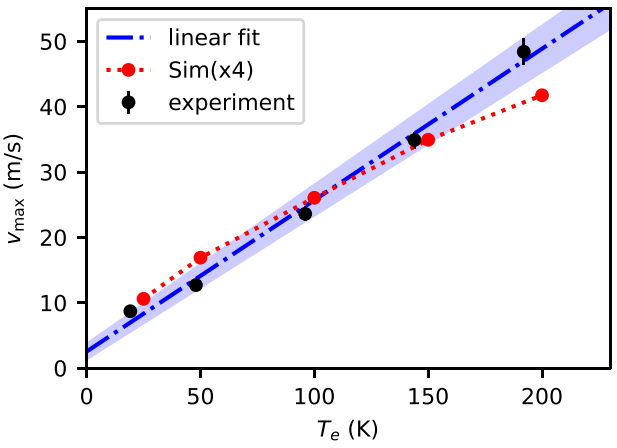

FIG. 3. Change in maximum velocity vs initial electron temperature in the first 25 ns of plasma evolution. The black circles are the experimental values, the blue dot-dashed line is a linear fit to the data, the shaded region represents the 1 σ estimate of the uncertainty in the fit. The red circles and dotted line show values from the simulation multiplied by a factor of 4. The BGK and LB simulation predict the same acceleration because they use the same electric field model.

$$\langle v_z(z)\rangle = \frac{\int v_z f(z, v_z)\, dv_z}{\int f(z, v_z)\, dv_z}. \tag{16}$$

The maximum excursions from zero velocity are plotted in Fig. 3. We analyze the simulation data in the same way, averaging the velocity distribution over the first 25 ns and calculating the hydrodynamic velocity using Eq. (16). These data are also shown in Fig. 3.

Both the experiment and the simulation reveal a linear dependence of the ion acceleration on the initial electron temperature. The simulations underpredict the initial acceleration, as expected. However, this underprediction is inconsequential in the overall plasma evolution, because the electrons quickly thermalize. The electron density model in Eq. (10) is a good approximation for most of the plasma evolution.

C. Thermalization

In Fig. 4, we compare the rms velocity of the ion distribution function in the center of the gap along the z (longitudinal) and y (transverse) directions. When the counterstreaming plasmas have merged, we extract the rms width by fitting the fluorescence line shape, $S(y, z, \nu)$, to a Voigt profile,

$$S(y, z, \nu) = a\,\mathrm{Re}\{w[\tilde{z} - \tilde{\nu}_0(y, z)]\}, \tag{17}$$

where $\tilde{z} - \tilde{\nu}_0(y, z) = [\nu - \nu_0(y, z) + i\gamma]/[\sigma(y, z)\sqrt{2}]$ and $w[x]$ is the Faddeeva function. The Voigt profile is the convolution of a Lorentzian and Gaussian line shape. The isolated atom line shape is Lorentzian. The measured laser-induced fluorescence line shape convolves the velocity distribution with the atomic response. When the velocity distribution is Gaussian, fitting the fluorescence line shape to the Voigt profile allows us to extract the underlying rms Gaussian velocity width. In the fit, we use the amplitude a, the center frequency $\nu_0(y, z)$, and the rms Gaussian width $\sigma(y, z)$ as fit parameters. We use this method to determine v_{rms} for all the y axis data in Fig. 4 and also for the z axis data after 5 μs.

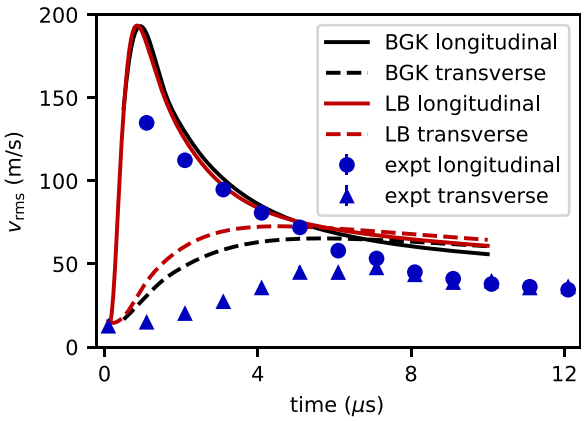

FIG. 4. The rms velocity (the square-root of the second centered moment) of the ion distribution function in the z (longitudinal) and y (transverse) directions. The experimental data are shown in blue circles and triangles. The experimental and simulation longitudinal data are similar. The transverse broadening rates show a wider discrepancy.

On the other hand, when the distribution function contains multiple peaks, we calculate the rms velocity using from the fluorescence line shape

$$v_{z,\mathrm{rms}}(z) = \left[\frac{\int_{-\infty}^{\infty} (v_z - u_z)^2 S(z, v_z)\, dv_z}{\int_{-\infty}^{\infty} S(z, v_z)\, dv_z}\right]^{1/2}, \tag{18}$$

where u_z is the z-component of the hydrodynamic velocity. We use this method for the z axis data in Fig. 4 for $0 < t < 5\,\mu$ s. Using Eq. (18) overestimates the rms velocity because of fluorescence measurements automatically include a convolution of the velocity distribution with the atomic line shape. However, in the data of Fig. 4, the power-broadened Lorentzian half-width corresponds to a velocity of 6.9 m/s. For the multi-peaked distributions earlier than 5 μs in Figs. 2 and 4, this additional broadening is negligible.

The data in Fig. 4 provide insights into the details of the kinetic simulations. In the longitudinal direction, the simulations match each other and the experiment for the second moment of the velocity distribution. In the transverse direction, the simulations overpredict the broadening of the second moment. This is likely due to the isotropic nature of the collision model's treatment of post-collisional velocities. The BGK model assumes a spherical Gaussian post-collision velocity distribution. An improved model that used an ellipsoidal distribution would better capture scattering in the direction of particle motion.[94,95] Similarly for LB, which broadens the fastest in Fig. 4, an improved model would allow for non-symmetric diffusion tensor.[96]

In the experiment and both simulations, we verify that the transverse distribution functions are nearly Maxwellian at all times. However, the longitudinal distributions are more complicated. In the experiment, the bimodal nature of the longitudinal velocity distribution in the center of the plasma has relaxed by 5 μs [see Fig. 2(a)] and reached a local equilibrium by 7 μs (see Fig. 4). A similar situation is true for the LB simulation. However, the BGK simulation has not fully relaxed by 7 μs.

VI. DISCUSSION

One of the aims of this study is to probe the validity of kinetic models compared to a simple, well-characterized experiment, one in which the initial ion density, electron temperature, spatial density profile, and charge state are known. In both the BGK and LB simulations, the approach to thermalization is much slower than in the experiment. This is evident in both Figs. 2 and 4. This discrepancy likely stems from fundamental limitations in both kinetic models. The BGK model approximates the collision operator by relaxing the distribution function toward a local Maxwellian at a single characteristic rate. It considers only the first three velocity moments (density, momentum, and energy) and assumes these moments adequately capture the essential physics of thermalization. For example, the second moment of the velocity distribution in the longitudinal direction matches the experiment in Fig. 4. However, this simplified treatment may not properly account for the complex velocity-space structures that develop in strongly-coupled plasmas with steep gradients.

The Lenard–Bernstein operator introduces velocity-space diffusion and friction, potentially capturing some additional physics missing from BGK. However, it uses only the same low-order moments to

define these terms. It also relies on a factorized collision frequency that may not accurately represent the true collision processes in our system. The velocity-space derivatives in LB help describe the smoothing of sharp features in the distribution function. In our hands, the LB model over predicts the relaxation of counterpropagating ion flow.

Our electric field model, based on Poisson–Boltzmann in Eq. (12), treats electrons as a fluid rather than a kinetic species. While this assumption significantly improves computational efficiency, it may oversimplify the electron response to density gradients. The fluid treatment cannot capture non-Maxwellian features in the electron distribution function that could affect ion thermalization through modified screening and electric field fluctuations.

Several factors could contribute to observed discrepancies between the simulations and the experiment and also between the two simulations.

- The assumption of a single relaxation time in BGK may be too simplistic, as different moments of the distribution function might relax at different rates in strongly coupled systems.
- Both models account for strong coupling effects that could enhance thermalization through collective modes only implicitly, through the SMT collision cross-sections.
- The use of only three moments in BGK might miss important higher order effects that become relevant when density gradients are steep.
- Both kinetic models derive from a perturbative expansion of the Boltzmann equation. BGK is derived using an expansion around an equilibrium distribution, plus further approximations. LB derives from the Fokker–Planck equation, which approximates the collision physics assuming small angle scattering. These perturbative approaches may not be valid for our highly non-equilibrium plasma in the gap.
- The factorized collision frequencies in both models may not capture the full velocity dependence of the actual collision processes and collision cross sections.
- The fluid treatment of electrons may miss important kinetic effects in the electron response that could modify the electric field and affect ion thermalization.

An extended BGK model (EBGK) that includes additional moments and a more sophisticated treatment of the collision frequency might better match the experimental results. Additionally, treating electrons kinetically, while computationally intensive, could provide insight into whether electron kinetic effects significantly influence the thermalization rate. However, the observed discrepancies suggest that new theoretical approaches may be needed to fully describe thermalization in strongly coupled plasmas with steep gradients.

With a better model, future work could focus on more complex interface structures, such as a sharply pointed triangular gap, or systems in which the plasma density varied significantly on either side of the gap. Adding the possibility of binary ion mixtures further enriches the HEDP applicability of future studies.

ACKNOWLEDGMENTS

This work was supported in part by the National Science Foundation (Grant Nos. NSF-2009999 and NSF-2108505). This work was supported in part by the U.S. Department of Energy through the Los Alamos National Laboratory. Los Alamos National Laboratory is operated by Triad National Security, LLC, for the National Nuclear Security Administration of U.S. Department of Energy (Contract No. 89233218CNA000001).

AUTHOR DECLARATIONS

Conflict of Interest

The authors have no conflicts to disclose.

Author Contributions

Scott Bergeson: Conceptualization (equal); Data curation (equal); Formal analysis (equal); Funding acquisition (equal); Investigation (equal); Methodology (equal); Project administration (equal); Resources (equal); Software (equal); Supervision (equal); Validation (equal); Visualization (equal); Writing – original draft (equal); Writing – review & editing (equal). **Matthew Schlitters:** Data curation (equal); Investigation (equal). **Matthew Miller:** Data curation (equal); Investigation (equal). **Ben Farley:** Data curation (equal); Investigation (equal). **Devin Sieverts:** Data curation (equal); Formal analysis (equal); Investigation (equal). **Michael S. Murillo:** Conceptualization (equal); Formal analysis (equal); Investigation (equal); Methodology (equal); Software (equal); Supervision (equal); Validation (equal); Writing – review & editing (equal). **Jeffrey R. Haack:** Formal analysis (equal); Investigation (equal); Methodology (equal); Resources (equal); Software (equal); Validation (equal); Visualization (equal); Writing – review & editing (equal).

DATA AVAILABILITY

The data that support the findings of this study are available from the corresponding author upon reasonable request.

REFERENCES

[1]C. A. Williams, R. Betti, V. Gopalaswamy, J. P. Knauer, C. J. Forrest, A. Lees, R. Ejaz, P. S. Farmakis, D. Cao, P. B. Radha *et al.*, "Demonstration of hot-spot fuel gain exceeding unity in direct-drive inertial confinement fusion implosions," Nat. Phys. **20**(5), 758–764 (2024).
[2]V. Gopalaswamy, C. A. Williams, R. Betti, D. Patel, J. P. Knauer, A. Lees, D. Cao, E. M. Campbell, P. Farmakis, R. Ejaz *et al.*, "Demonstration of a hydrodynamically equivalent burning plasma in direct-drive inertial confinement fusion," Nat. Phys. **20**(5), 751–757 (2024).
[3]H. Abu-Shawareb, R. Acree, P. Adams, J. Adams, B. Addis, R. Aden, P. Adrian, B. B. Afeyan, M. Aggleton, L. Aghaian *et al.*, "Lawson criterion for ignition exceeded in an inertial fusion experiment," Phys. Rev. Lett. **129**, 075001 (2022).
[4]A. L. Kritcher, A. B. Zylstra, D. A. Callahan, O. A. Hurricane, C. R. Weber, D. S. Clark, C. V. Young, J. E. Ralph, D. T. Casey, A. Pak *et al.*, "Design of an inertial fusion experiment exceeding the Lawson criterion for ignition," Phys. Rev. E **106**, 025201 (2022).
[5]V. Tikhonchuk, "A boost for laser fusion," Nat. Phys. **20**(5), 682–683 (2024).
[6]S. X. Hu, K. A. Nichols, N. R. Shaffer, B. Arnold, A. J. White, L. A. Collins, V. V. Karasiev, S. Zhang, V. N. Goncharov, R. C. Shah, D. I. Mihaylov, S. Jiang, and Y. Ping, "A review on charged-particle transport modeling for laser direct-drive fusion," Phys. Plasmas **31**(4), 040501 (2024).
[7]D. J. Schlossberg, G. P. Grim, D. T. Casey, A. S. Moore, R. Nora, B. Bachmann, L. R. Benedetti, R. M. Bionta, M. J. Eckart, J. E. Field, D. N. Fittinghoff, M. Gatu Johnson, V. Geppert-Kleinrath, E. P. Hartouni, R. Hatarik, W. W. Hsing, L. C. Jarrott, S. F. Khan, J. D. Kilkenny, O. L. Landen, B. J. MacGowan, A. J. Mackinnon, K. D. Meaney, D. H. Munro, S. R. Nagel, A. Pak, P. K. Patel, B. K. Spears, P. L. Volegov, and C. V. Young, "Observation of hydrodynamic flows

in imploding fusion plasmas on the National Ignition Facility," Phys. Rev. Lett. **127**, 125001 (2021).
[8]B. Keenan, *Verification Study of xRAGE's Multi-Ion Viscosity Model* [Office of Scientific and Technical Information (OSTI), 2022].
[9]I. V. Igumenshchev, V. N. Goncharov, F. J. Marshall, J. P. Knauer, E. M. Campbell, C. J. Forrest, D. H. Froula, V. Y. Glebov, R. L. McCrory, S. P. Regan, T. C. Sangster, S. Skupsky, and C. Stoeckl, "Three-dimensional modeling of direct-drive cryogenic implosions on OMEGA," Phys. Plasmas **23**(5), 052702 (2016).
[10]T. J. B. Collins, C. Stoeckl, R. Epstein, W. A. Bittle, C. J. Forrest, V. Y. Glebov, V. N. Goncharov, D. R. Harding, S. X. Hu, D. W. Jacobs-Perkins, T. Z. Kosc, J. A. Marozas, C. Mileham, F. J. Marshall, S. F. B. Morse, P. B. Radha, S. P. Regan, B. Rice, T. C. Sangster, M. J. Shoup, W. T. Shmayda, C. Sorce, W. Theobald, and M. D. Wittman, "Causes of fuel–ablator mix inferred from modeling of monochromatic time-gated radiography of OMEGA cryogenic implosions," Phys. Plasmas **29**(1), 012702 (2022).
[11]B. M. Haines, "Charged particle transport coefficient challenges in high energy density plasmas," Phys. Plasmas **31**(5), 050501 (2024).
[12]S. P. Regan, V. N. Goncharov, T. C. Sangster, E. M. Campbell, R. Betti, J. W. Bates, K. Bauer, T. Bernat, S. Bhandarkar, T. R. Boehly *et al.*, "The national direct-drive inertial confinement fusion program," Nucl. Fusion **59**(3), 032007 (2019).
[13]S. E. Anderson, L. Chacón, A. N. Simakov, B. M. Haines, and D. S. Montgomery, "Validation of hydrodynamic and kinetic simulations with a plasma interpenetration ICF hohlraum experiment," arXiv:2403.04967 (2024).
[14]J. Castro, P. McQuillen, and T. C. Killian, "Ion acoustic waves in ultracold neutral plasmas," Phys. Rev. Lett. **105**, 065004 (2010).
[15]P. McQuillen, J. Castro, S. J. Bradshaw, and T. C. Killian, "Emergence of kinetic behavior in streaming ultracold neutral plasmas," Phys. Plasmas **22**(4), 043514 (2015).
[16]G. Bannasch, J. Castro, P. McQuillen, T. Pohl, and T. C. Killian, "Velocity relaxation in a strongly coupled plasma," Phys. Rev. Lett. **109**, 185008 (2012).
[17]V. S. Dharodi and M. S. Murillo, "Sculpted ultracold neutral plasmas," Phys. Rev. E **101**, 023207 (2020).
[18]S. D. Bergeson, S. D. Baalrud, C. Leland Ellison, E. Grant, F. R. Graziani, T. C. Killian, M. S. Murillo, J. L. Roberts, and L. G. Stanton, "Exploring the crossover between high-energy-density plasma and ultracold neutral plasma physics," Phys. Plasmas **26**(10), 100501 (2019).
[19]R. T. Farouki and S. Hamaguchi, "Thermodynamics of strongly-coupled Yukawa systems near the one-component-plasma limit. II. Molecular dynamics simulations," J. Chem. Phys **101**(11), 9885 (1994).
[20]M. Baus and J.-P. Hansen, "Statistical mechanics of simple coulomb systems," Phys. Rep. **59**(1), 1 (1980).
[21]L. G. Stanton and M. S. Murillo, "Ionic transport in high-energy-density matter," Phys. Rev. E **93**, 043203 (2016).
[22]B. Jeon, M. Foster, J. Colgan, G. Csanak, J. D. Kress, L. A. Collins, and N. Grønbech-Jensen, "Energy relaxation rates in dense hydrogen plasmas," Phys. Rev. E **78**, 036403 (2008).
[23]B. Xu and S. X. Hu, "Effects of electron-ion temperature equilibration on inertial confinement fusion implosions," Phys. Rev. E **84**, 016408 (2011).
[24]Q. Ma, J. Dai, D. Kang, M. S. Murillo, Y. Hou, Z. Zhao, and J. Yuan, "Extremely low electron-ion temperature relaxation rates in warm dense hydrogen: Interplay between quantum electrons and coupled ions," Phys. Rev. Lett. **122**, 015001 (2019).
[25]G. Dimonte and J. Daligault, "Molecular-dynamics simulations of electron-ion temperature relaxation in a classical Coulomb plasma," Phys. Rev. Lett. **101**, 135001 (2008).
[26]F. R. Graziani, V. S. Batista, L. X. Benedict, J. I. Castor, H. Chen, S. N. Chen, C. A. Fichtl, J. N. Glosli, P. E. Grabowski, A. T. Graf *et al.*, "Large-scale molecular dynamics simulations of dense plasmas: The Cimarron Project," High Energy Density Phys. **8**(1), 105–131 (2012).
[27]G. Faussurier, "Electron-ion coupling factor for temperature relaxation in dense plasmas," Phys. Rev. E **101**, 023206 (2020).
[28]D. O. Gericke, M. S. Murillo, and M. Schlanges, "Dense plasma temperature equilibration in the binary collision approximation," Phys. Rev. E **65**, 036418 (2002).
[29]L. Brown, D. Preston, and R. Singleton, Jr. "Charged particle motion in a highly ionized plasma," Phys. Rep. **410**(4), 237–333 (2005).
[30]S. Rightley and S. D. Baalrud, "Kinetic model for electron-ion transport in warm dense matter," Phys. Rev. E **103**, 063206 (2021).
[31]L. B. Fletcher, J. Vorberger, W. Schumaker, C. Ruyer, S. Goede, E. Galtier, U. Zastrau, E. P. Alves, S. D. Baalrud, R. A. Baggott, B. Barbrel, Z. Chen, T. Döppner, M. Gauthier, E. Granados, J. B. Kim, D. Kraus, H. J. Lee, M. J. MacDonald, R. Mishra, A. Pelka, A. Ravasio, C. Roedel, A. R. Fry, R. Redmer, F. Fiuza, D. O. Gericke, and S. H. Glenzer, "Electron-ion temperature relaxation in warm dense hydrogen observed with picosecond resolved X-ray scattering," Front. Phys. **10**, 838524 (2022).
[32]C.-Z. Gao, C.-B. Zhang, Y. Cai, Y. Wu, Z.-F. Fan, P. Wang, and J.-G. Wang, "Assessment of the electron-proton energy relaxation rates extracted from molecular dynamics simulations in weakly-coupled hydrogen plasmas," Phys. Rev. E **107**, 015203 (2023).
[33]Y. S. Lavrinenko, I. V. Morozov, and I. A. Valuev, "Electron–ion temperature relaxation in nonideal plasmas: High accuracy classical molecular dynamics simulations," Contrib. Plasma Phys. **64**(5), 202300158 (2024).
[34]R. Redmer and G. Röpke, "Progress in the theory of dense strongly coupled plasmas," Contrib. Plasma Phys. **50**(10), 970–985 (2010).
[35]P. K. Shukla, A. A. Mamun, and D. A. Mendis, "Nonlinear ion modes in a dense plasma with strongly coupled ions and degenerate electron fluids," Phys. Rev. E **84**, 026405 (2011).
[36]S. Hamaguchi, R. T. Farouki, and D. H. E. Dubin, "Triple point of Yukawa systems," Phys. Rev. E **56**, 4671–4682 (1997).
[37]O. Vaulina, S. Khrapak, and G. Morfill, "Universal scaling in complex (dusty) plasmas," Phys. Rev. E **66**, 016404 (2002).
[38]E. E. Salpeter and H. M. Van Horn, "Nuclear reaction rates at high densities," Astrophys. J. **155**, 183 (1969).
[39]D. Stevenson, "The condensed matter physics of planetary interiors," J. Phys. Colloq. **41**, 53 (1980).
[40]B. A. Remington, R. P. Drake, and D. D. Ryutov, "Experimental astrophysics with high power lasers and *Z* pinches," Rev. Mod. Phys. **78**, 755 (2006).
[41]H. Abu-Shawareb, R. Acree, P. Adams, J. Adams, B. Addis, R. Aden, P. Adrian, B. B. Afeyan, M. Aggleton, L. Aghaian *et al.*, "Achievement of target gain larger than unity in an inertial fusion experiment," Phys. Rev. Lett. **132**, 065102 (2024).
[42]M. A. Liberman, J. S. De Groot, A. Toor, and R. B. Spielman, *Physics of High-Density Z-Pinch Plasmas* (Springer New York, 1999).
[43]H. Thomas, G. E. Morfill, V. Demmel, J. Goree, B. Feuerbacher, and D. Möhlmann, "Plasma crystal: Coulomb crystallization in a dusty plasma," Phys. Rev. Lett. **73**, 652–655 (1994).
[44]J. Beckers, J. Berndt, D. Block, M. Bonitz, P. J. Bruggeman, L. Couëdel, G. L. Delzanno, Y. Feng, R. Gopalakrishnan, F. Greiner *et al.*, "Physics and applications of dusty plasmas: The perspectives 2023," Phys. Plasmas **30**(12), 120601 (2023).
[45]E. Shuryak, "Strongly coupled quark-gluon plasma in heavy ion collisions," Rev. Mod. Phys. **89**, 035001 (2017).
[46]W.-j. Fu, J. M. Pawlowski, and F. Rennecke, "QCD phase structure at finite temperature and density," Phys. Rev. D **101**(5), 054032 (2020).
[47]P. K. Shukla and A. A. Mamun, *Introduction to Dusty Plasma Physics* (CRC Press, 2015).
[48]A. Schella, M. Mulsow, and A. Melzer, "Correlation buildup during recrystallization in three-dimensional dusty plasma clusters," Phys. Plasmas **21**, 050701 (2014).
[49]A. Piel and A. Melzer, "Dynamical processes in complex plasmas," Plasma Phys. Control. Fusion **44**(1), R1–R26 (2002).
[50]M. Bonitz, C. Henning, and D. Block, "Complex plasmas: A laboratory for strong correlations," Rep. Prog. Phys. **73**(6), 066501 (2010).
[51]D. H. E. Dubin and T. M. O'Neil, "Trapped nonneutral plasmas, liquids, and crystals (the thermal equilibrium states)," Rev. Mod. Phys. **71**, 87–172 (1999).
[52]X.-P. Huang, F. Anderegg, E. M. Hollmann, C. F. Driscoll, and T. M. O'Neil, "Steady-state confinement of non-neutral plasmas by rotating electric fields," Phys. Rev. Lett. **78**, 875–878 (1997).
[53]M. J. Jensen, T. Hasegawa, J. J. Bollinger, and D. H. E. Dubin, "Rapid heating of a strongly coupled plasma near the solid-liquid phase transition," Phys. Rev. Lett. **94**, 025001 (2005).

[54]T. C. Killian, T. Pattard, T. Pohl, and J. M. Rost, "Ultracold neutral plasmas," Phys. Rep. **449**(4–5), 77–130 (2007).
[55]M. Lyon and S. L. Rolston, "Ultracold neutral plasmas," Rep. Prog. Phys. **80**(1), 017001 (2017).
[56]M. K. Warrens, N. P. Inman, G. M. Gorman, B. T. Husick, S. J. Bradshaw, and T. C. Killian, "Wave steepening and shock formation in ultracold neutral plasmas," Phys. Plasmas **31**(11), 113503 (2024).
[57]T. S. Strickler, T. K. Langin, P. McQuillen, J. Daligault, and T. C. Killian, "Experimental measurement of self-diffusion in a strongly coupled plasma," Phys. Rev. X **6**, 021021 (2016).
[58]A. S. Richardson, "2019 NRL plasma formulary," Technical report, US Naval Research Laboratory, 2019.
[59]L. X. Benedict, M. P. Surh, J. I. Castor, S. A. Khairallah, H. D. Whitley, D. F. Richards, J. N. Glosli, M. S. Murillo, C. R. Scullard, P. E. Grabowski, D. Michta, and F. R. Graziani, "Molecular dynamics simulations and generalized Lenard-Balescu calculations of electron-ion temperature equilibration in plasmas," Phys. Rev. E **86**, 046406 (2012).
[60]P. E. Grabowski, S. B. Hansen, M. S. Murillo, L. G. Stanton, F. R. Graziani, A. B. Zylstra, S. D. Baalrud, P. Arnault, A. D. Baczewski, L. X. Benedict *et al.*, "Review of the first charged-particle transport coefficient comparison workshop," High Energy Density Phys. **37**, 100905 (2020).
[61]L. J. Stanek, A. Kononov, S. B. Hansen, B. M. Haines, S. X. Hu, P. F. Knapp, M. S. Murillo, L. G. Stanton, H. D. Whitley, S. D. Baalrud *et al.*, "Review of the second charged-particle transport coefficient code comparison workshop," Phys. Plasmas **31**(5), 052104 (2024).
[62]M. S. Murillo, "Viscosity estimates of liquid metals and warm dense matter using the Yukawa reference system," High Energy Density Phys. **4**(1–2), 49–57 (2008).
[63]T. C. Killian and S. L. Rolston, "Ultracold neutral plasmas," Phys. Today **63**(3), 46–51 (2010).
[64]R. Tucker Sprenkle, L. G. Silvestri, M. S. Murillo, and S. D. Bergeson, "Temperature relaxation in strongly-coupled binary ionic mixtures," Nat. Commun. **13**(1), 15 (2022).
[65]L. G. Silvestri, R. Tucker Sprenkle, S. D. Bergeson, and M. M. Murillo, "Relaxation of strongly coupled binary ionic mixtures in the coupled mode regime," Phys. Plasmas **28**(6), 062302 (2021).
[66]R. Tucker Sprenkle, S. D. Bergeson, L. G. Silvestri, and M. S. Murillo, "Ultracold neutral plasma expansion in a strong uniform magnetic field," Phys. Rev. E **105**, 045201 (2022).
[67]E. V. Crockett, R. C. Newell, F. Robicheaux, and D. A. Tate, "Heating and cooling of electrons in an ultracold neutral plasma using Rydberg atoms," Phys. Rev. A **98**, 043431 (2018).
[68]T. K. Langin, G. M. Gorman, and T. C. Killian, "Laser cooling of ions in a neutral plasma," Science **363**(6422), 61–64 (2019).
[69]M. A. Viray, S. A. Miller, and G. Raithel, "Coulomb expansion of a cold non-neutral rubidium plasma," Phys. Rev. A **102**, 033303 (2020).
[70]T. Kroker, M. Großmann, K. Sengstock, M. Drescher, P. Wessels-Staarmann, and J. Simonet, "Ultrafast electron cooling in an expanding ultracold plasma," Nat. Commun. **12**(1), 596 (2021).
[71]L. G. Stanton, S. D. Bergeson, and M. S. Murillo, "Transport in non-ideal, multi-species plasmas," Phys. Plasmas **28**(5), 050401 (2021).
[72]T. Sprenkle, A. Dodson, E. McKnight, R. Spencer, S. Bergeson, A. Diaw, and M. S. Murillo, "Ion friction at small values of the Coulomb logarithm," Phys. Rev. E **99**, 053206 (2019).
[73]P. McQuillen, T. Strickler, T. Langin, and T. C. Killian, "Ion temperature evolution in an ultracold neutral plasma," Phys. Plasmas **22**(3), 033513 (2015).
[74]W.-T. Chen, C. Witte, and J. L. Roberts, "Observation of a strong-coupling effect on electron-ion collisions in ultracold plasmas," Phys. Rev. E **96**, 013203 (2017).
[75]P. Jiang and J. L. Roberts, "Electric field influences on the initial electron temperature of ultracold plasmas," Phys. Plasmas **26**(4), 043513 (2019).
[76]M. Aghigh, K. Grant, R. Haenel, K. L. Marroquín, F. B. V. Martins, H. Sadegi, M. Schulz-Weiling, J. Sous, R. Wang, J. S. Keller, and E. R. Grant, "Dissipative dynamics of atomic and molecular Rydberg gases: Avalanche to ultracold plasma states of strong coupling," J. Phys. B: At. Mol. Opt. Phys. **53**(7), 074003 (2020).
[77]J. Sous and E. Grant, "Possible many-body localization in a long-lived finite-temperature ultracold quasineutral molecular plasma," Phys. Rev. Lett. **120**, 110601 (2018).
[78]M. Lyon, S. D. Bergeson, and M. S. Murillo, "Limit of strong ion coupling due to electron shielding," Phys. Rev. E **87**(3), 033101 (2013).
[79]M. Lyon, S. D. Bergeson, A. Diaw, and M. S. Murillo, "Using higher ionization states to increase coulomb coupling in an ultracold neutral plasma," Phys. Rev. E **91**(3), 033101 (2015).
[80]M. Lyon, S. D. Bergeson, G. Hart, and M. S. Murillo, "Strongly-coupled plasmas formed from laser-heated solids," Sci. Rep. **5**, 15693 (2015).
[81]M. S. Murillo and S. D. Bergeson, "Ultracold neutral plasmas well into the strongly coupled regime," in *Advances in Atomic, Molecular, and Optical Physics* (Elsevier, 2015), pp. 223–271.
[82]C. Pak, V. Billings, M. Schlitters, S. D. Bergeson, and M. S. Murillo, "Preliminary study of plasma modes and electron-ion collisions in partially magnetized strongly coupled plasmas," Phys. Rev. E **109**, 015201 (2024).
[83]M. Schlitters, M. Miller, B. Farley, and S. D. Bergeson, "Comment on 'Ultracold plasma expansion in quadrupole magnetic field,'" Phys. Rev. E **110**, 027201 (2024).
[84]M. Mills, P. Puri, Y. Yu, A. Derevianko, C. Schneider, and E. R. Hudson, "Efficient repumping of a Ca magneto-optical trap," Phys. Rev. A **96**, 033402 (2017).
[85]T. K. Langin, T. Strickler, N. Maksimovic, P. McQuillen, T. Pohl, D. Vrinceanu, and T. C. Killian, "Demonstrating universal scaling for dynamics of Yukawa one-component plasmas after an interaction quench," Phys. Rev. E **93**, 023201 (2016).
[86]Y. C. Chen, C. E. Simien, S. Laha, P. Gupta, Y. N. Martinez, P. G. Mickelson, S. B. Nagel, and T. C. Killian, "Electron screening and kinetic-energy oscillations in a strongly coupled plasma," Phys. Rev. Lett. **93**, 265003 (2004).
[87]S. Laha, P. Gupta, C. E. Simien, H. Gao, J. Castro, T. Pohl, and T. C. Killian, "Experimental realization of an exact solution to the Vlasov equations for an expanding plasma," Phys. Rev. Lett. **99**, 155001 (2007).
[88]E. A. Cummings, J. E. Daily, D. S. Durfee, and S. D. Bergeson, "Fluorescence measurements of expanding strongly coupled neutral plasmas," Phys. Rev. Lett. **95**, 235001 (2005).
[89]P. L. Bhatnagar, E. P. Gross, and M. Krook, "A model for collision processes in gases. I. Small amplitude processes in charged and neutral one-component systems," Phys. Rev. **94**, 511–525 (1954).
[90]J. R. Haack, C. D. Hauck, and M. S. Murillo, "Interfacial mixing in high-energy-density matter with a multiphysics kinetic model," Phys. Rev. E **96**, 063310 (2017).
[91]T. Chuna, I. Sagert, M. S. Murillo, and J. R. Haack, "Multi-species kinetic-fluid coupling for high-energy density simulations," J. Comput. Phys. **505**, 112908 (2024).
[92]A. Lenard and I. B. Bernstein, "Plasma oscillations with diffusion in velocity space," Phys. Rev. **112**, 1456–1459 (1958).
[93]J. R. Haack, C. D. Hauck, and M. S. Murillo, "A conservative, entropic multi-species BGK model," J. Stat. Phys. **168**(4), 826–856 (2017).
[94]L. H. Holway, Jr. "Kinetic theory of shock structure using an ellipsoidal distribution function," in *Rarefied Gas Dynamics*, edited by J. H. de Leeuw (Academic Press, New York, 1965), Vol. 1, p. 193.
[95]H. Struchtrup and P. Taheri, "Macroscopic transport models for rarefied gas flows: A brief review," IMA J. Appl. Math. **76**(5), 672–697 (2011).
[96]J. Mathiaud and L. Mieussens, "A Fokker–Planck model of the Boltzmann equation with correct Prandtl number," J. Stat. Phys. **162**(2), 397–414 (2016).